Attosecond and femtosecond forces exerted on gold nanoparticles induced by swift electrons

Maureen J. Lagos,[1,*] Alejandro Reyes-Coronado,[2] Andrea Konečná,[3] Pedro M. Echenique,[3]
Javier Aizpurua,[3] and Philip E. Batson[1,†]
[1]*Institute for Advanced Materials, Devices, and Nanotechnology, Rutgers University, Piscataway, New Jersey 08854, USA*
[2]*Departamento de Física, Facultad de Ciencias, Universidad Nacional Autónoma de México, Mexico City, 04510, Mexico*
[3]*Center for Materials Physics (CSIC-UPV/EHU) and Donostia International Physics Center, "DIPC," Donostia-San Sebastian, 20018, Spain*
(Received 22 October 2015; revised manuscript received 18 April 2016; published 31 May 2016)

We report time-dependent calculations of attosecond and femtosecond forces imposed by a kilovolt swift electron during passage near a nanometer-sized metal particle. Contrary to expectations based on dielectric theory, which suggest that the forces should always be attractive, we find that for very close approaches, attosecond forces are repulsive, and are caused by interaction of the magnetic field of the relativistic electron with currents within even nominally nonmagnetic nanoparticles. These results suggest an explanation for the observation of both attractive and repulsive nanoparticle movement during the first use of Ångstrom-sized electron beams in electron microscopy.

DOI: 10.1103/PhysRevB.93.205440

I. INTRODUCTION

The interaction of light and electrons with nanoscale structures underpins the fascinating field of plasmonics, which seeks to understand and engineer useful subwavelength optical behavior [1,2]. While spectroscopic tools dominate studies of resonant structure, fast optical pump and electron probe experiments have revealed rich femtosecond transient behavior [3,4]. Kilovolt electrons also carry ultrafast electromagnetic fields which couple strongly to nanostructures, producing electron energy loss scattering [5–7] and lateral momentum transfer [8]. We report numerical results for the spatial and temporal behavior of lateral electromagnetic forces within a gold nanoparticle, to identify physical mechanisms for both attractive and repulsive manipulation of nanoparticles, recently observed using Ångstrom-sized electron beams [8,9].

Characterization of nanostructures using optical and electron microscopies often creates nanoscale changes, suggesting methods for deliberate manipulation of very small objects. For instance, trapping an atom in an ultracold state relies on light-matter mechanical coupling under laser illumination [10]. Optical tweezers, based on momentum transfer during light scattering, allow the trapping of submicron-sized particles [11]. While these techniques offer a wide range of capabilities in different size ranges, it is still difficult to deliberately manipulate objects at the atomic and nanoscale levels [12]. Recently it has been found that an electron beam can be used to deliberately manipulate metal nanoparticles, even producing both attractive and repulsive forces [8,9,13–16].

With the development of modern aberration-corrected scanning transmission electron microscopes we can routinely make and precisely control atom-sized electron beams [17]. Placement of this probe extremely close to a nanoparticle (NP), without intersecting the NP boundaries, produces momentum transfer to the NP by interaction with the electromagnetic fields associated with the passing electron. This "aloof" scattering apparently drives both attractive and repulsive forces between the electron beam and single NPs depending on details of the electron passage [8,15]. Attractive forces are easy to understand in a simple dielectric model, but the remarkable observation of a transition between pulling and pushing behavior of single gold NPs, as the electron beam approaches the NP, has not been understood. Numerical modeling in the frequency domain has shown the existence of a crossover between pulling and pushing, as the impact parameter is made smaller, in carbon fullerenes [18] and gold NPs [9]. However, the physical origin of repulsive forces driven by the interaction of a charged particle with a nonmagnetic dielectric object has not been explained.

For common electron beam currents of a few tens of picoamperes, in modern electron microscopes, there is essentially a single electron present in the microscope at any one moment in time. At energies above about 50 keV, electron de Broglie wavelengths are two orders of magnitude smaller than the Ångstrom scale. Under these circumstances quantum corrections (Heisenberg broadening) can be neglected for relativistic electrons [19–21]. Also, for aloof scattering near a NP, lateral momentum transfer is small relative to the momentum carried by the swift electron, so scattering angles are very small. Thus, in Fig. 1 we used classical electrodynamics to describe the interaction of a relativistic electron traveling in a linear trajectory having an impact parameter b away from the surface of a metal NP.

II. THEORETICAL APPROACH

Forces responsible for the NP movement result from interactions between the moving charges inside the NP and external electromagnetic fields associated with the passing electron. In this section we present the approach used to calculate the time-dependent electromagnetic forces and fields.

A. Calculation of time-dependent forces and fields

We have followed the method suggested by Barnett and Loudon [22] to calculate the Lorentz forces acting on a

*maureen.lagos@rutgers.edu
†batson@physics.rutgers.edu

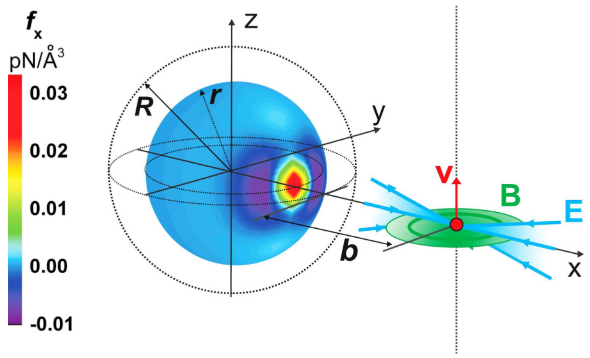

FIG. 1. The electromagnetic interaction between a traveling relativistic electron (red dot) and a spherical nanoparticle (NP) of radius R in an aloof geometry. Both attractive and repulsive electromagnetic forces are generated in the NP, illustrated through the X component of the force density (f_x) map plotted over an inner spherical shell of radius r.

dielectric object, and then use Newton's second law to calculate the momentum transfer. The time-dependent Lorentz force $\vec{F}(t)$ can be obtained directly from time-dependent total fields acting on charges ρ and currents $\vec{J}$ within the NP volume V [23]:

$$\vec{F}(t) = \frac{d\vec{P}_{\text{mech}}(t)}{dt} = \int_V (\rho\vec{E} + \vec{J} \times \vec{B})dV, \tag{1}$$

where $\vec{E}$ and $\vec{B}$ represent the fundamental time-varying electric and magnetic fields and dV is a differential volume within the NP. Using Maxwell's equations, charge and current densities can be replaced by electric and magnetic fields, leading to the following representation [23]:

$$\vec{F}(t) = \int_V \left\{\varepsilon_0[\vec{E}(\nabla\cdot\vec{E}) - \vec{E}\times(\nabla\times\vec{E})] + \frac{1}{\mu_0}[\vec{B}(\nabla\cdot\vec{B}) - \vec{B}\times(\nabla\times\vec{B})] - \varepsilon_0\left[\frac{\partial}{\partial t}(\vec{E}\times\vec{B})\right]\right\}dV, \tag{2}$$

where ε_0 is the vacuum permittivity and μ_0 is the vacuum permeability. The integrand in Eq. (2) is the Lorentz force density, which we have used to analyze the spatial distribution of instantaneous forces acting on a nanosized particle [see for instance Figs. 1, 2(a), and 3]. Details about the calculations of the electromagnetic fields are presented in the Appendix.

We studied the electromagnetic interaction between a metal NP (gold and aluminum) and energetic fast electrons (80 and 120 keV) moving with several impact parameters (between 1 and 50 Å). We present here only the results of the forces and fields acting on a gold 1 nm radius NP induced by 120 keV electron to describe our general findings.

B. Dielectric response function

We characterize the gold NP with an experimentally determined dielectric response which agrees well with theory [24,25]. We have interpolated the experimental data using a cubic spline in order to produce a uniform grid for Fourier analysis over 4 keV, enforcing the causality principle through a Kramers-Kronig analysis. The experimental data for the dielectric response function includes damping and information of both low energy surface and bulk plasmons (~2.5–2.8 eV),

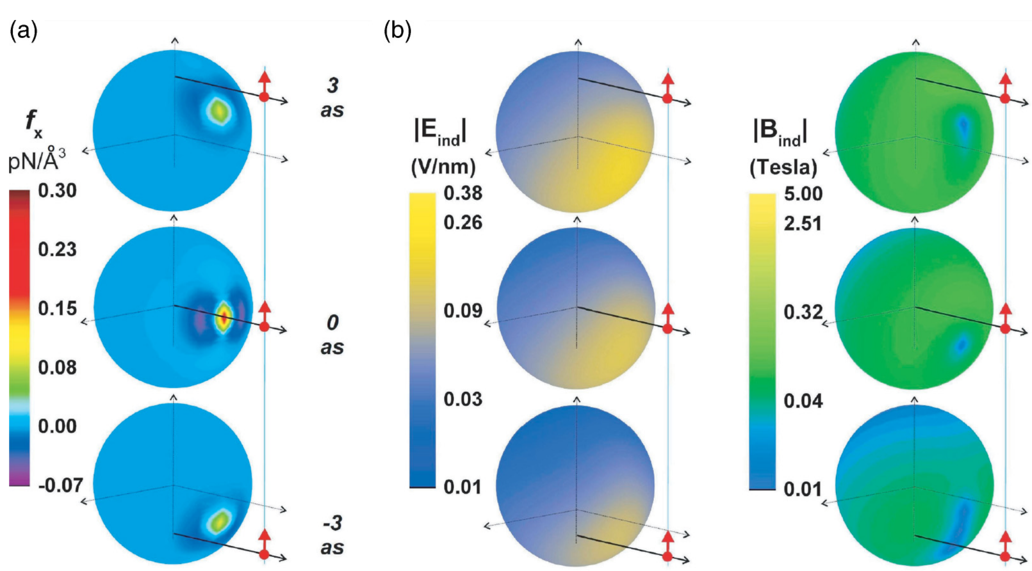

FIG. 2. Temporal dynamics of forces and fields in a nanometer particle. (a) Sequence of three-dimensional images (perspective view) of the force density during the transit of the aloof electron. The electron position is indicated by a red dot and arrow at different times ($t = -3$, 0, and 3 as). (b) Sequence of three-dimensional images (perspective view) of the modulus of induced electric (left side) and magnetic (right side) fields, corresponding to the same events shown in (a). Note that induced fields lag the relativistic electron and exhibit variations within attosecond times. See text for explanation.

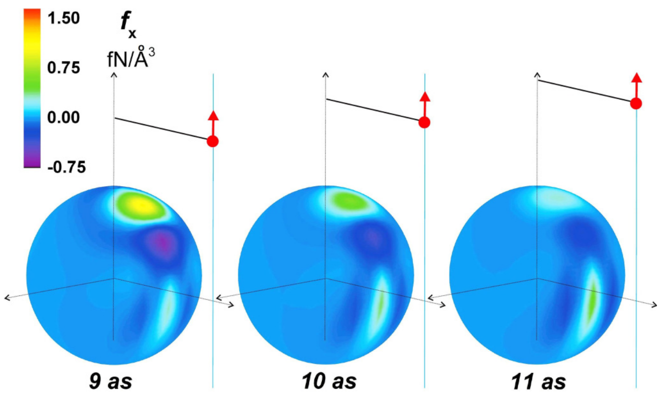

FIG. 3. Lorentz forces acting on the sphere exhibit a wakelike structure within attosecond times. The pattern is confined in the nanoparticle and follows the passing electron. Note that the regions of finite forces display a conelike pattern spreading over the surface in the transverse direction to the electron trajectory.

and higher energy instabilities (∼25 eV), associated with $5d \rightarrow 6f$ electron transitions, which apparently include strong collective behavior [24,25]. The presence of a ∼25 eV collective response is suggested by a narrow minimum in the real part of the tabulated dielectric constant, accompanied by a small dissipation.

III. RESULTS

We focus on the transverse X component of the forces to explore the detailed physics behind the movement of metal NPs driven by the electron beam [13–16].

A. Temporal evolution of forces and fields

In Fig. 2 we show the instantaneous force density and fields acting on a spherical shell ($r = 0.9$ nm) just below the surface of the NP. The forces and fields in other regions of the NP volume follow the same trend. The fast electron travels in an aloof geometry with impact parameter of 5 Å. The aloof electron positions are indicated by a red dot at different times.

Figures 2(a) and 2(b) show the time evolution of the Lorentz force density and induced fields, respectively. In Fig. 2(a), different regions of the NP are subjected to attractive or repulsive forces, so that the total Lorentz force on the NP at a particular time results from the competition between positive and negative contributions. In general, we find that attractive forces are largely dielectric, while repulsive forces are strongly associated with the magnetic fields produced by the keV electron, even for aluminum, a nonmagnetic material.

We notice that the NP response fields increase gradually during the approach of the fast electron, reflecting the long range nature of the external fields. During these times [$t < 0$ as in Fig. 2(a)] force densities are primarily dielectric, exhibiting a dipolelike configuration, with an attractive part oriented towards the fast electron [left side of Fig. 2(b)] and a weaker repulsive part behind the NP (not seen in this perspective). The response magnetic fields [right side of Fig. 2(b)] display a donutlike pattern surrounding the dielectric response, with an elongated central region of almost-zero field. As the electron passes ($t \sim 0$ as), the patterns of force density exhibit very strong regions of attractive dielectric forces accompanied by two lateral lobes of repulsive magnetic forces. Later ($t > 0$ as), the spatially confined NP charges lag behind the traveling electron, and a spatial separation of the positive correlation charge from the accompanying negative charge pileup in front the correlation hole is produced [21,26,27]. During this time, positive, attractive forces decrease, while magnetically driven negative forces become more important. Snapshots at $t = 3$ as show that these negative magnetic forces become tightly grouped around the highly localized, attractive dielectric forces.

As the electron moves away from the NP ($t > 5$ as), this interplay of forces creates a pattern that resembles a moving charge density wake on the NP surface (Fig. 3). It is well known that two different types of spatial patterns associated with plasmon excitations can be generated by swift charged particles: bow and trailing wakes [21,26,27]. Note in Fig. 3 the alternating trail of positive and negative forces with a wavelength of roughly 1.5 nm, much smaller than the typical surface or bulk plasmon wavelengths of 20–40 nm when driven by keV electrons. This suggests that the spatial behavior here is limited by the NP size. During these very short times, the interaction between the fast electron and moving charges results in a broad region of negative forces which opposes the attractive contribution [see Fig. 4(a), $t > 5$ as].

Lorentz forces at attosecond times can be treated as gradient field forces acting on induced charge distributions inside the NP. The main contribution to the forces can be described, in a first approximation, by the dipole mode $\nabla(\vec{E} \cdot \vec{p})$ and $\nabla(\vec{B} \cdot \vec{m})$, where $\vec{p}$ and $\vec{m}$ are the instantaneous polarization and magnetization vectors, respectively [23]. However, at a very small impact parameter when high field gradients are present at the NP, strong nondipole response charge distributions are also excited [28]. We find that these higher order modes further weaken the dielectric contribution to the total momentum transfer (see Sec. III C).

As the electron moves well past the NP ($t > 50$ as) external fields near the NP become very small, and the response field at the NP collapses, giving rise to plasmon oscillations within the NP. At these times, the oscillatory total electric field strength (∼mV/nm) is about three orders of magnitude smaller than at the attosecond times (∼V/nm), which consequently produces plasmon-based electric forces that are at least six orders magnitude smaller than the attosecond impulse forces [compare Figs. 4(a) and 4(b)].

B. Attosecond and femtosecond forces acting on nanoparticles

Figure 4 shows the total lateral Lorentz forces integrated over the volume of the NP for impact parameters 1.5, 5, and 10 Å (black, red, and blue, respectively). In Fig. 4(a) we see that during the close approach, the total forces are impulselike with instantaneous peak strengths of a few piconewtons (pN), lasting about 11 as for this case, controlled by the electron motion during the close approach. We find that attractive forces are primarily dielectric and occur during the swift electron approach for $t < 0$ as. The total forces become negative as the electron moves away for $t > 0$ as, driven by increasing magnetic contributions.

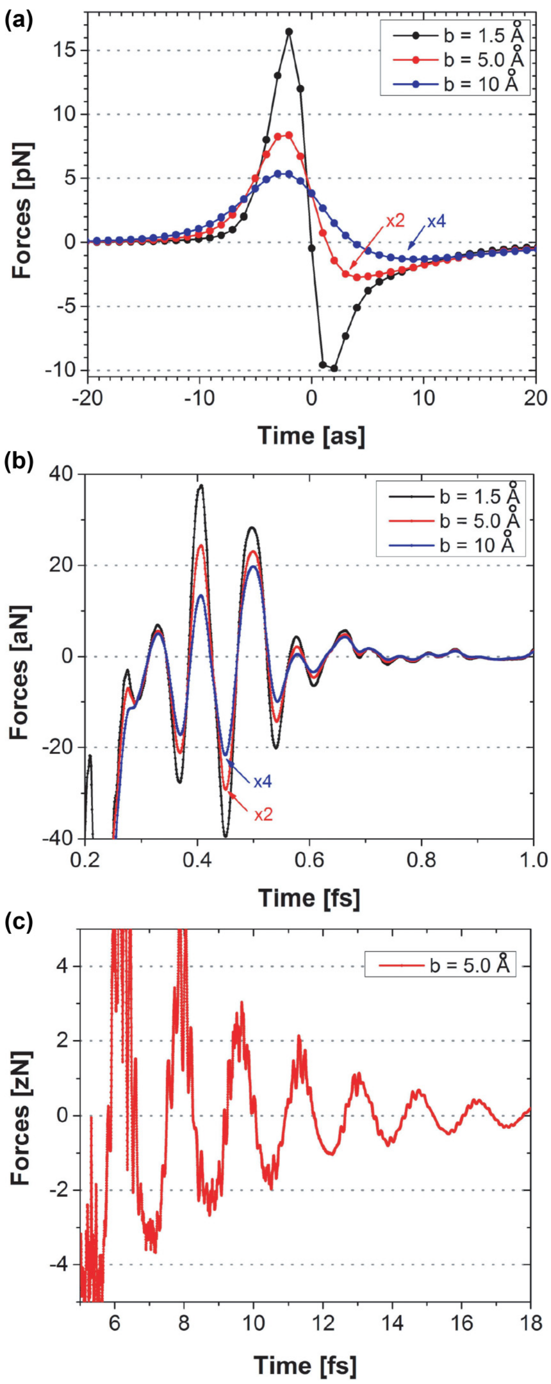

FIG. 4. Time-dependent Lorentz forces in the X direction for impact parameters 1.5 Å (black curve), 5 Å (red curve), and 10 Å (blue curve). The red and blue curves were multiplied by a constant factor for better visualization. (a) Attosecond impulse forces during the close passage of the swift electron, showing both attractive and repulsive behavior as a function of impact parameter. (b) Oscillatory, subfemtosecond forces at ultraviolet energies. (c) Forces originating in surface plasmons in the visible range for the 5 Å impact parameter.

Figures 4(b) and 4(c) show a damped oscillatory behavior resulting from plasmonic modes at femtosecond times. Within the first femtosecond [Fig. 4(b)] the oscillatory force has a period of about 0.17 fs associated with a high-energy plasmon instability (∼25 eV). This instability has been noted in theoretical calculations and is likely collective behavior associated with $5d \rightarrow 6f$ electron transitions [25]. Later in time [Fig. 4(c)] oscillatory forces are dominated by a lower energy mode (∼2.5 eV) with a 1.7 fs period, corresponding to the optical surface plasmons for the gold nanosphere. The ∼25 eV deep ultraviolet modes continue to be visible, overlapping with the lower energy surface plasmon related forces. Plasmonic forces are likely to be associated with photon emission, which would join the electromagnetic fields surrounding the NP [9,29,30].

C. Total momentum transfer

Integrating the forces over time, we find that total time-average attractive forces are larger than repulsive forces at large impact parameter ($b > 5$ Å), but become comparable at small impact parameter ($b < 5$ Å), leading to a crossover from attractive to repulsive behavior, in agreement with frequency domain calculations [9,18]. Figure 5(a) shows our results associated with the transverse component of the total momentum transfer (TMT) calculated in both time and frequency domain. From the law of momentum conservation the time-averaged TMT [blue curve in Fig. 5(b)] can be easily understood to be the result of the competition between positive electric [black curve in Fig. 5(b)] and negative magnetic [red curve in Fig. 5(b)] contributions. The fact that the magnetic field gives a negative contribution is in agreement with our description as diamagneticlike repulsive forces. Also, our analysis of the relative contributions of the impulse attosecond and oscillatory femtosecond forces to the TMT showed that most of the significant contribution comes from the impulse forces acting in the attosecond range. For all of the cases, plasmonic fields contribute less than ∼7%. This consequently implies that the impact parameter dependence of the TMT which causes the transition to repulsive forces is dictated mainly by the attosecond forces during the close approach of the swift electron.

To get more insight into the physical origin of the repulsion at small impact parameters, we analyzed the role of both dipole and higher mode induced fields to the TMT. Our result shows that the higher modes (quadrupole, octupole, etc.) mainly weaken the electric contribution (EC) at short distances ($b < 5$ Å), leaving the magnetic contribution largely unchanged. This behavior agrees with our physical intuition because the excitation of higher modes spreads regions of positive response charges away from areas immediately beneath the swift electron, leading to a weakening of attractive dielectric forces. For larger impact parameters ($b > 5$ Å) the forces are dominated by the excitation of dipole fields, which produce the expected attractive behavior.

In addition, Fig. 5(c) shows attosecond Lorentz forces calculated considering a relativistic electron traveling with impact parameter of 1.5 Å. The orange and black curves correspond to forces obtained using the dipole mode ($l = 1$) and several mode ($l = 1$–20) contributions, respectively. The dipolar result includes a strong attractive peak during the electron approach ($t < 1$ as) and a small repulsive component ($t > 1$ as). From the physical picture of dielectric and diamagneticlike forces in the dipole approximation it is expected

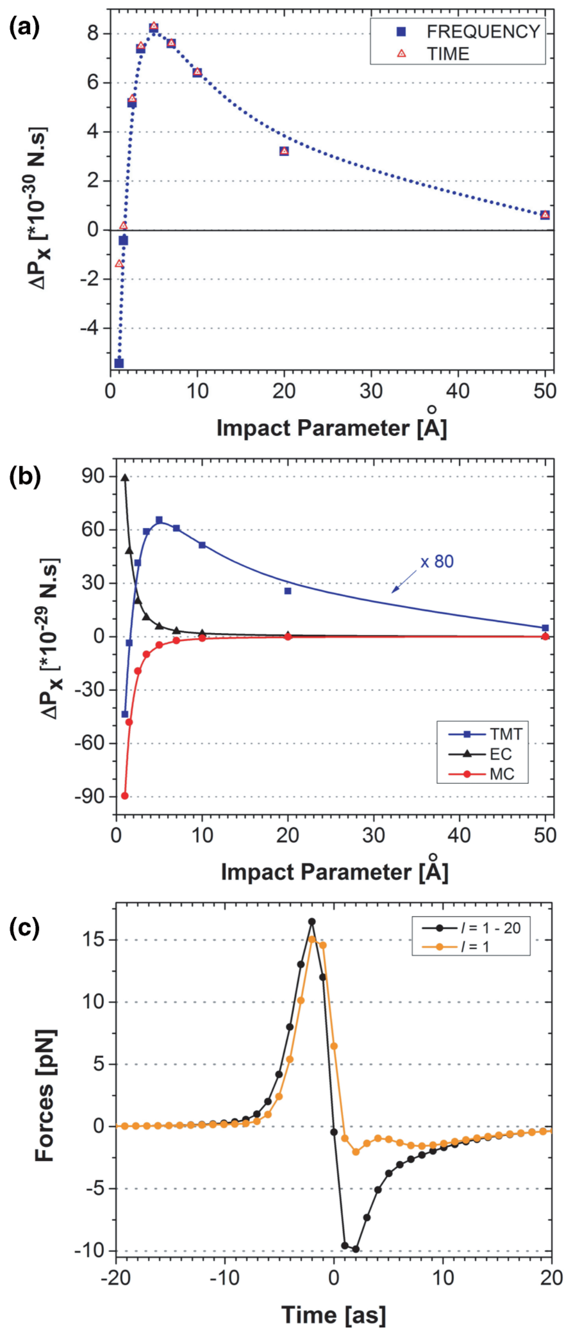

FIG. 5. (a) Transverse component of the total momentum transfer (TMT) as a function of impact parameter, calculated using both time-dependent and frequency-dependent fields. (b) The electric (EC) and magnetic (MC) contributions to the TMT are displayed in black and red, respectively. The blue curve associated with the TMT was multiplied by 80 to render a better visualization. (c) Time-dependent forces calculated considering the dipole mode (orange curve) and several modes (black curve) of the induced fields, driven by a passing 120 keV electron with impact parameter of 1.5 Å. Note that the enhancement of the repulsive behavior ($t > 0$ as) is caused by high-order mode contribution in the attosecond range.

that the attractive contributions are mainly dominated by the dielectric interaction, while the repulsive one is mainly driven by the diamagnetic interaction. The multipole result (black curve), in contrast, includes a significant increase of the repulsion ($t > 1$ as). This substantial change is caused by a weakening of the electric contribution to the TMT during the formation of the complicated wake patterns formed at attosecond times, discussed with Fig. 3 above.

IV. CONCLUSIONS

Attosecond Lorentz forces are thus an important consequence of a close approach by a relativistic electron, and result from large gradients of external electric and magnetic fields across the nanoparticle. While attractive dielectric forces are expected for slow electrons, repulsive magnetic contributions can dominate behavior for relativistic electrons. Later at femtosecond times, oscillatory forces are possible through plasmon decay by photon emission. The two behaviors are apparently bridged by a wakelike structure which occurs a few attoseconds after passage of the electron, and which later collapses, producing the lower energy surface and bulk oscillatory plasmon modes. We have noticed an interesting plasmon instability in gold near 25 eV. These results bring understanding to the physics of repulsive and attractive force behavior between nonmagnetic metal NPs and swift electrons. We also think that this detailed understanding suggests opportunities for systematic experimental work in the future towards better understanding of ultrafast behavior of nanoscale structures.

ACKNOWLEDGMENTS

M.J.L. and P.E.B. acknowledge support from the U.S. Department of Energy, Office of Science, Basic Energy Sciences under Award No. DE-SC0005132. J.A., A.K., and P.M.E. acknowledge support from the Spanish Ministry of Economy and Competitiveness MINECO under the Project FIS2013-41184-P. A.R.C. acknowledges financial support from DGAPA/PAPIIT-UNAM project, Grant IA105015.

APPENDIX: ELECTROMAGNETIC FIELDS

The swift passing electron probes the spherical object in an aloof geometry as shown in Fig. 1, traveling parallel to the Z axis. The electron is represented by a red dot moving with a speed v with an impact parameter of b. In this spherical geometry, the frequency-dependent response fields in the sphere can be calculated using a multipolar expansion, satisfying boundary conditions on the surface of the spherical NP, and they are presented as follows (where CGS-atomic units are used). A detailed description of the derivation of expressions associated with the frequency-dependent electromagnetic fields is found in Refs. [9,18]. These expressions include retardation and relativistic effects which allow us to capture the physics of the high-speed events:

1. Induced fields outside the spherical particle

$$
\begin{aligned}
\vec{\mathbf{E}}^{\text{ind,out}}(\mathbf{r},\omega) = {}& \mathbf{e}_r \frac{2\pi\omega}{c^2\gamma}\sum_{l=1}^{\infty}\sum_{m=-l}^{l} t_l^{\mathrm{E}}\frac{h_l^{(1)}(kr)}{kr}B_{l,m}K_m\left(\frac{\omega\xi}{v\gamma}\right)Y_{l,m}(\theta,\phi)\\
&-\mathbf{e}_\theta\left\{\frac{4\pi\omega v}{c^3}\sum_{l=1}^{\infty}\sum_{m=-l}^{l}\frac{t_l^{\mathrm{M}}m^2}{l(l+1)\sin\theta}h_l^{(1)}(kr)A_{l,m}^{+}K_m\left(\frac{\omega\xi}{v\gamma}\right)Y_{l,m}(\theta,\phi)\right.\\
&+\frac{2\pi\omega}{c^2\gamma}\sum_{l=1}^{\infty}\sum_{m=-l}^{l}\frac{t_l^{\mathrm{E}}}{l(l+1)}B_{l,m}K_m\left(\frac{\omega\xi}{v\gamma}\right)\left[(l+1)\frac{h_l^{(1)}(kr)}{kr}-h_{l+1}^{(1)}(kr)\right]\\
&\left.\times\left[\frac{(l+1)\cos\theta}{\sin\theta}Y_{l,m}(\theta,\phi)-\frac{(l-m+1)}{\sin\theta}\frac{\alpha_{l,m}}{\alpha_{l+1,m}}Y_{l+1,m}(\theta,\phi)\right]\right\}\\
&+\mathbf{e}_\phi\left\{\frac{4\pi\mathrm{i}\omega v}{c^3}\sum_{l=1}^{\infty}\sum_{m=-l}^{l}\frac{t_l^{\mathrm{M}}m}{l(l+1)}h_l^{(1)}(kr)A_{l,m}^{+}K_m\left(\frac{\omega\xi}{v\gamma}\right)\left[\frac{(l+1)\cos\theta}{\sin\theta}Y_{l,m}(\theta,\phi)-\frac{(l-m+1)}{\sin\theta}\frac{\alpha_{l,m}}{\alpha_{l+1,m}}Y_{l+1,m}(\theta,\phi)\right]\right.\\
&\left.+\frac{2\pi\mathrm{i}\omega}{c^2\gamma}\sum_{l=1}^{\infty}\sum_{m=-l}^{l}\frac{t_l^{\mathrm{E}}m}{l(l+1)\sin\theta}B_{l,m}K_m\left(\frac{\omega\xi}{v\gamma}\right)Y_{l,m}(\theta,\phi)\left[(l+1)\frac{h_l^{(1)}(kr)}{kr}-h_{l+1}^{(1)}(kr)\right]\right\},
\end{aligned}
\tag{A1}
$$

$$
\begin{aligned}
\vec{\mathbf{B}}^{\text{ind,out}}(\mathbf{r},\omega) = {}& \mathbf{e}_r \frac{4\pi\omega v}{c^3}\sum_{l=1}^{\infty}\sum_{m=-l}^{l} t_l^{\mathrm{M}}m\frac{h_l^{(1)}(kr)}{kr}A_{l,m}^{+}K_m\left(\frac{\omega\xi}{v\gamma}\right)Y_{l,m}(\theta,\phi)\\
&+\mathbf{e}_\theta\left\{\frac{2\pi\omega}{c^2\gamma}\sum_{l=1}^{\infty}\sum_{m=-l}^{l}\frac{t_l^{\mathrm{E}}m}{l(l+1)\sin\theta}h_l^{(1)}(kr)B_{l,m}K_m\left(\frac{\omega\xi}{v\gamma}\right)Y_{l,m}(\theta,\phi)\right.\\
&-\frac{4\pi\omega v}{c^3}\sum_{l=1}^{\infty}\sum_{m=-l}^{l}\frac{t_l^{\mathrm{M}}m}{l(l+1)}A_{l,m}^{+}K_m\left(\frac{\omega\xi}{v\gamma}\right)\left[(l+1)\frac{h_l^{(1)}(kr)}{kr}-h_{l+1}^{(1)}(kr)\right]\\
&\left.\times\left[\frac{(l+1)\cos\theta}{\sin\theta}Y_{l,m}(\theta,\phi)-\frac{(l-m+1)}{\sin\theta}\frac{\alpha_{l,m}}{\alpha_{l+1,m}}Y_{l+1,m}(\theta,\phi)\right]\right\}\\
&-\mathbf{e}_\phi\left\{\frac{2\pi\mathrm{i}\omega}{c^2\gamma}\sum_{l=1}^{\infty}\sum_{m=-l}^{l}\frac{t_l^{\mathrm{E}}}{l(l+1)}h_l^{(1)}(kr)B_{l,m}K_m\left(\frac{\omega\xi}{v\gamma}\right)\left[\frac{(l+1)\cos\theta}{\sin\theta}Y_{l,m}(\theta,\phi)-\frac{(l-m+1)}{\sin\theta}\frac{\alpha_{l,m}}{\alpha_{l+1,m}}Y_{l+1,m}(\theta,\phi)\right]\right.\\
&\left.-\frac{4\pi\mathrm{i}\omega v}{c^3}\sum_{l=1}^{\infty}\sum_{m=-l}^{l}\frac{t_l^{\mathrm{M}}m^2}{l(l+1)\sin\theta}A_{l,m}^{+}K_m\left(\frac{\omega\xi}{v\gamma}\right)Y_{l,m}(\theta,\phi)\left[(l+1)\frac{h_l^{(1)}(kr)}{kr}-h_{l+1}^{(1)}(kr)\right]\right\}.
\end{aligned}
\tag{A2}
$$

2. Induced fields inside the spherical particle

$$
\begin{aligned}
\vec{\mathbf{E}}^{\text{ind,in}}(\mathbf{r},\omega) = {}& \mathbf{e}_r \frac{-2\pi\mathrm{i}\omega}{c^2\gamma}\sum_{l=1}^{\infty}\left(s_l^{\mathrm{E}}\frac{j_l(k_{\mathrm{in}}r)}{k_{\mathrm{in}}r}-\frac{j_l(kr)}{kr}\right)\sum_{m=-l}^{l}B_{l,m}K_m\left(\frac{\omega\xi}{v\gamma}\right)Y_{l,m}(\theta,\phi)\\
&+\mathbf{e}_\theta\left\{\frac{4\pi\mathrm{i}\omega v}{c^3}\sum_{l=1}^{\infty}\left[s_l^{\mathrm{M}}j_l(k_{\mathrm{in}}r)-j_l(kr)\right]\sum_{m=-l}^{l}\frac{m^2}{l(l+1)\sin\theta}A_{l,m}^{+}K_m\left(\frac{\omega\xi}{v\gamma}\right)Y_{l,m}(\theta,\phi)\right.\\
&+\frac{2\pi\mathrm{i}\omega}{c^2\gamma}\sum_{l=1}^{\infty}\frac{1}{l(l+1)}\sum_{m=-l}^{l}B_{l,m}K_m\left(\frac{\omega\xi}{v\gamma}\right)\left[s_l^{\mathrm{E}}\left((l+1)\frac{j_l(k_{\mathrm{in}}r)}{k_{\mathrm{in}}r}-j_{l+1}(k_{\mathrm{in}}r)\right)-\left((l+1)\frac{j_l(kr)}{kr}-j_{l+1}(kr)\right)\right]\\
&\left.\times\left[\frac{(l+1)\cos\theta}{\sin\theta}Y_{l,m}(\theta,\phi)-\frac{(l-m+1)}{\sin\theta}\frac{\alpha_{l,m}}{\alpha_{l+1,m}}Y_{l+1,m}(\theta,\phi)\right]\right\}\\
&+\mathbf{e}_\phi\left\{\frac{4\pi\omega v}{c^3}\sum_{l=1}^{\infty}\frac{s_l^{\mathrm{M}}j_l(k_{\mathrm{in}}r)-j_l(kr)}{l(l+1)}\sum_{m=-l}^{l}mA_{l,m}^{+}K_m\left(\frac{\omega\xi}{v\gamma}\right)\right.
\end{aligned}
$$

$$\times\left[\frac{(l+1)\cos\theta}{\sin\theta}Y_{l,m}(\theta,\phi)-\frac{(l-m+1)}{\sin\theta}\frac{\alpha_{l,m}}{\alpha_{l+1,m}}Y_{l+1,m}(\theta,\phi)\right]$$
$$+\frac{2\pi\omega}{c^2\gamma}\sum_{l=1}^{\infty}\frac{1}{l(l+1)}\sum_{m=-l}^{l}\frac{m}{\sin\theta}B_{l,m}K_m\left(\frac{\omega\xi}{v\gamma}\right)Y_{l,m}(\theta,\phi)$$
$$\times\left[s_l^{\mathrm{E}}\left((l+1)\frac{j_l(k_{\mathrm{in}}r)}{k_{\mathrm{in}}r}-j_{l+1}(k_{\mathrm{in}}r)\right)-\left((l+1)\frac{j_l(kr)}{kr}-j_{l+1}(kr)\right)\right]\Bigg\},\tag{A3}$$

$$\vec{\mathbf{B}}^{\mathrm{ind,in}}(\mathbf{r},\omega)=\mathbf{e}_r\frac{-4\pi\mathrm{i}\omega v\sqrt{\varepsilon_\mathrm{r}}}{c^3}\sum_{l=1}^{\infty}\left(s_l^{\mathrm{M}}\frac{j_l(k_{\mathrm{in}}r)}{k_{\mathrm{in}}r}-\frac{1}{\sqrt{\varepsilon_\mathrm{r}}}\frac{j_l(kr)}{kr}\right)\sum_{m=-l}^{l}mA^+_{l,m}K_m\left(\frac{\omega\xi}{v\gamma}\right)Y_{l,m}(\theta,\phi)$$
$$+\mathbf{e}_\theta\Bigg\{\frac{-2\pi\mathrm{i}\omega\sqrt{\varepsilon_\mathrm{r}}}{c^2\gamma}\sum_{l=1}^{\infty}\left(s_l^{\mathrm{E}}j_l(k_{\mathrm{in}}r)-\frac{j_l(kr)}{\sqrt{\varepsilon_\mathrm{r}}}\right)\sum_{m=-l}^{l}\frac{\vec{B}_{l,m}}{l(l+1)}\frac{m}{\sin\theta}K_m\left(\frac{\omega\xi}{v\gamma}\right)Y_{l,m}(\theta,\phi)$$
$$+\frac{4\pi\mathrm{i}\omega v\sqrt{\varepsilon_\mathrm{r}}}{c^3}\sum_{l=1}^{\infty}\frac{1}{l(l+1)}\sum_{m=-l}^{l}mA^+_{l,m}K_m\left(\frac{\omega\xi}{v\gamma}\right)\left[\frac{(l+1)\cos\theta}{\sin\theta}Y_{l,m}(\theta,\phi)-\frac{(l-m+1)}{\sin\theta}\frac{\alpha_{l,m}}{\alpha_{l+1,m}}Y_{l+1,m}(\theta,\phi)\right]$$
$$\times\left[s_l^{\mathrm{M}}\left((l+1)\frac{j_l(k_{\mathrm{in}}r)}{k_{\mathrm{in}}r}-j_{l+1}(k_{\mathrm{in}}r)\right)-\frac{1}{\sqrt{\varepsilon_\mathrm{r}}}\left((l+1)\frac{j_l(kr)}{kr}-j_{l+1}(kr)\right)\right]\Bigg\}$$
$$-\mathbf{e}_\phi\Bigg\{\frac{2\pi\omega\sqrt{\varepsilon_\mathrm{r}}}{c^2\gamma}\sum_{l=1}^{\infty}\left(s_l^{\mathrm{E}}j_l(k_{\mathrm{in}}r)-\frac{j_l(kr)}{\sqrt{\varepsilon_\mathrm{r}}}\right)\sum_{m=-l}^{l}\frac{\vec{B}_{l,m}}{l(l+1)}K_m\left(\frac{\omega\xi}{v\gamma}\right)$$
$$\times\left[\frac{(l+1)\cos\theta}{\sin\theta}Y_{l,m}(\theta,\phi)-\frac{(l-m+1)}{\sin\theta}\frac{\alpha_{l,m}}{\alpha_{l+1,m}}Y_{l+1,m}(\theta,\phi)\right]$$
$$-\frac{4\pi\omega v\sqrt{\varepsilon_\mathrm{r}}}{c^3}\sum_{l=1}^{\infty}\frac{1}{l(l+1)}\sum_{m=-l}^{l}\frac{m^2}{\sin\theta}A^+_{l,m}K_m\left(\frac{\omega\xi}{v\gamma}\right)Y_{l,m}(\theta,\phi)$$
$$\times\left[s_l^{\mathrm{M}}\left((l+1)\frac{j_l(k_{\mathrm{in}}r)}{k_{\mathrm{in}}r}-j_{l+1}(k_{\mathrm{in}}r)\right)-\frac{1}{\sqrt{\varepsilon_\mathrm{r}}}\left((l+1)\frac{j_l(kr)}{kr}-j_{l+1}(kr)\right)\right]\Bigg\},\tag{A4}$$

where

$$\xi=R+b,\tag{A5}$$

where R is the sphere radius and b is the impact parameter. The Lorentz factor γ is expressed by

$$\gamma=\frac{1}{\sqrt{1-\beta^2}},\tag{A6}$$

and the β constant defined as

$$\beta=\frac{v}{c}.\tag{A7}$$

The coefficients $A^+_{l,m}$ are evaluated using

$$A^+_{l,m}=\frac{1}{\beta^{l+1}}\sum_{j=m}^{l}\frac{\mathrm{i}^{l-j}\alpha_{l,m}(2l+1)!!}{\gamma^j2^j(l-j)![(j-m)/2]![(j+m)/2]!}\times I^{l,m}_{j,l-j},\tag{A8}$$

where

$$\alpha_{l,m}=\sqrt{\frac{2l+1}{4\pi}\frac{(l-m)!}{(l+m)!}}\tag{A9}$$

is associated with the definition of the spherical harmonics $Y_{l,m}(\theta,\phi)$, where θ is the azimuthal angle and ϕ is the polar angle. The numbers $I^{l,m}_{i_1,i_2}$ are calculated via the recurrence relation

$$(l-m)I^{l,m}_{i_1,i_2}=(2l-1)I^{l-1,m}_{i_1,i_2+1}-(l+m-1)I^{l-2,m}_{i_1,i_2},\tag{A10}$$

with the starting values

$$I^{m-1,m}_{i_1,i_2}=0,\tag{A11}$$

$$I^{m-2,m}_{i_1,i_2}=0,\tag{A12}$$

$$I^{m,m}_{i_1,i_2}=\begin{cases}(-1)^m(2m-1)!!B\left(\frac{i_1+m+2}{2},\frac{i_2+1}{2}\right), & \text{if } i_2 \text{ is even},\\ 0, & \text{if } i_2 \text{ is odd}.\end{cases}\tag{A13}$$

$B(x,y)$ is the beta function. The coefficients $B_{l,m}$ are calculated using $A^+_{l,m}$:

$$B_{l,m}=A^+_{l,m+1}\sqrt{(l+m+1)(l-m)}-A^+_{l,m-1}\sqrt{(l-m+1)(l+m)}.\tag{A14}$$

The following special functions are used in the calculation of the induced fields: spherical Bessel function of the first kind

$j_l(x)$, spherical Hankel function of the first kind $h_l^{(1)}(x)$, and modified Bessel function of the second kind $K_m(x)$ of order m.

The scattering coefficients are

$$t_l^{\mathrm{M}} = (-i)\frac{j_l(k_{\mathrm{in}}R)j_{l+1}(kR) - \sqrt{\varepsilon_{\mathrm{r}}}j_l(kR)j_{l+1}(k_{\mathrm{in}}R)}{\sqrt{\varepsilon_{\mathrm{r}}}j_{l+1}(k_{\mathrm{in}}R)h_l^{(1)}(kR) - j_l(k_{\mathrm{in}}R)h_{l+1}^{(1)}(kR)}, \tag{A15}$$

$$t_l^{\mathrm{E}} = (-i)\frac{\frac{(l+1)(1-\varepsilon_{\mathrm{r}})}{\sqrt{\varepsilon_{\mathrm{r}}}}j_l(kR)j_l(k_{\mathrm{in}}R) - kRj_l(kR)j_{l+1}(k_{\mathrm{in}}R) + k_{\mathrm{in}}Rj_l(k_{\mathrm{in}}R)j_{l+1}(kR)}{\frac{(l+1)(\varepsilon_{\mathrm{r}}-1)}{\sqrt{\varepsilon_{\mathrm{r}}}}j_l(k_{\mathrm{in}}R)h_l^{(1)}(kR) - k_{\mathrm{in}}Rj_l(k_{\mathrm{in}}R)h_{l+1}^{(1)}(kR) + kRj_{l+1}(k_{\mathrm{in}}R)h_l^{(1)}(kR)}, \tag{A16}$$

$$s_l^{\mathrm{M}} = \frac{j_{l+1}(kR)h_l^{(1)}(kR) - j_l(kR)h_{l+1}^{(1)}(kR)}{\sqrt{\varepsilon_{\mathrm{r}}}j_{l+1}(k_{\mathrm{in}}R)h_l^{(1)}(kR) - j_l(k_{\mathrm{in}}R)h_{l+1}^{(1)}(kR)}, \tag{A17}$$

$$s_l^{\mathrm{E}} = \frac{kRj_{l+1}(kR)h_l^{(1)}(kR) - kRj_l(kR)h_{l+1}^{(1)}(kR)}{\frac{(l+1)(\varepsilon_{\mathrm{r}}-1)}{\sqrt{\varepsilon_{\mathrm{r}}}}j_l(k_{\mathrm{in}}R)h_l^{(1)}(kR) - k_{\mathrm{in}}Rj_l(k_{\mathrm{in}}R)h_{l+1}^{(1)}(kR) + kRj_{l+1}(k_{\mathrm{in}}R)h_l^{(1)}(kR)}, \tag{A18}$$

where the wave vector is defined as $k = \omega/c$ and inside the sphere as $k_{\mathrm{in}} = \sqrt{\varepsilon_{\mathrm{r}}}k$. ε_{r} is the relative dielectric constant of the sphere.

3. External fields acting on the spherical particle

The external time-dependent electromagnetic fields associated with the relativistic electron are represented in the Cartesian coordinates (where SI units are used). Those fields can also be represented in the frequency domain, as shown in [9,18]

$$\begin{aligned}\vec{\mathbf{E}}^{\mathrm{ext}}(x,y,z,t) = &-\mathbf{e}_x\frac{e\gamma}{4\pi\varepsilon_0}\frac{x-\xi}{[(x-\xi)^2+y^2+\gamma^2(z-vt)^2]^{3/2}} - \mathbf{e}_y\frac{e\gamma}{4\pi\varepsilon_0}\frac{y}{[(x-\xi)^2+y^2+\gamma^2(z-vt)^2]^{3/2}}\\ &-\mathbf{e}_z\frac{e\gamma}{4\pi\varepsilon_0}\frac{z-vt}{[(x-\xi)^2+y^2+\gamma^2(z-vt)^2]^{3/2}},\end{aligned} \tag{A19}$$

$$\vec{\mathbf{B}}^{\mathrm{ext}}(x,y,z,t) = \mathbf{e}_x\frac{e\gamma}{4\pi\varepsilon_0}\frac{\beta}{c}\frac{y}{[(x-\xi)^2+y^2+\gamma^2(z-vt)^2]^{3/2}} - \mathbf{e}_y\frac{e\gamma}{4\pi\varepsilon_0}\frac{\beta}{c}\frac{x-\xi}{[(x-\xi)^2+y^2+\gamma^2(z-vt)^2]^{3/2}} + \mathbf{e}_z 0, \tag{A20}$$

where (x,y,z) represents a position in the Cartesian coordinates and e represents the fast electron charge. These analytical expressions can be also represented in spherical coordinates through a simple transformation of coordinates.

[1] J. A. Schuller, E. S. Barnard, W. Cai, Y. C. Jun, J. S. White, and M. L. Brongersma, Nat. Mater. **9**, 193 (2010).

[2] M. Kauranen and A. V. Zayats, Nat. Photon. **6**, 737 (2012).

[3] A. Yurtsever, R. M. van der Veen, and A. H. Zewail, Science **335**, 59 (2012).

[4] M. Balistreri, H. Gersen, J. Korterik, L. Kuipers, and N. Van Hulst, Science **294**, 1080 (2001).

[5] P. E. Batson, Phys. Rev. Lett. **49**, 936 (1982).

[6] J. Nelayah, M. Kociak, O. Stephan, F. J. García de Abajo, M. Tence, L. Henrard, D. Taverna, I. Pastoriza-Santos, L. M. Liz-Marzan, and C. Colliex, Nat. Phys. **3**, 348 (2007).

[7] M. Bosman, E. Ye, S. F. Tan, C. A. Nijhuis, J. K. W. Yang, R. Marty, A. Mlayah, A. Arbouet, C. Girard, and M.-Y. Han, Sci. Rep. **3**, 1312 (2013).

[8] P. E. Batson, A. Reyes-Coronado, R. Barrera, A. Rivacoba, P. Echenique, and J. Aizpurua, Nano Lett. **11**, 3388 (2011).

[9] A. Reyes-Coronado, R. G. Barrera, P. E. Batson, P. M. Echenique, A. Rivacoba, and J. Aizpurua, Phys. Rev. B **82**, 235429 (2010).

[10] D. Leibfried, R. Blatt, C. Monroe, and D. Wineland, Rev. Mod. Phys. **75**, 281 (2003).

[11] A. Ashkin, J. M. Dziedzic, J. E. Bjorkholm, and S. Chu, Opt. Lett. **11**, 288 (1986).

[12] O. M. Marago, P. H. Jones, P. G. Gucciardi, G. Volpe, and A. C. Ferrari, Nat. Nano. **8**, 807 (2013).

[13] H. Zheng, U. M. Mirsaidov, L.-W. Wang, and P. Matsudaira, Nano Lett. **12**, 5644 (2012).

[14] O. Cretu, J. Rodri-guez-Manzo, A. Demortiere, and F. Banhart, Carbon **50**, 259 (2012).

[15] P. E. Batson, A. Reyes-Coronado, R. Barrera, A. Rivacoba, P. Echenique, and J. Aizpurua, Ultramicroscopy **123**, 50 (2012).

[16] Y.-T. Chen, C.-Y. Wang, Y.-J. Hong, Y.-T. Kang, S.-E. Lai, P. Chang, and T.-R. Yew, RSC Adv. **4**, 31652 (2014).

[17] P. E. Batson, N. Dellby, and O. L. Krivanek, Nature (London) **418**, 617 (2002).

[18] F. J. García de Abajo, Phys. Rev. B **70**, 115422 (2004).

[19] R. H. Ritchie, Philos. Mag. A **44**, 931 (1981).

[20] R. H. Ritchie and A. Howie, Philos. Mag. A **58**, 753 (1988).

[21] P. M. Echenique, R. H. Ritchie, and W. Brandt, Phys. Rev. B **20**, 2567 (1979).

[22] S. M. Barnett and R. Loudon, Philos. Trans. R. Soc. London Sect. A **368**, 927 (2010).

[23] J. D. Jackson, *Classical Electrodynamics* (Wiley, New York, 1999).

[24] E. Palik, *Handbook of Optical Constants of Solids* (Academic, New York, 1985).

[25] I. Gurtubay, J. Pitarke, I. Campillo, and A. Rubio, Comput. Mater. Sci. **22**, 123 (2001).
[26] F. J. García de Abajo and P. M. Echenique, Phys. Rev. B **46**, 2663 (1992).
[27] M. Quijada, A. G. Borisov, I. Nagy, R. Díez Muiño, and P. M. Echenique, Phys. Rev. A **75**, 042902 (2007).
[28] T. L. Ferrell and P. M. Echenique, Phys. Rev. Lett. **55**, 1526 (1985).
[29] J. Crowell and R. H. Ritchie, Phys. Rev. **172**, 436 (1968).
[30] F. J. García de Abajo and A. Howie, Phys. Rev. Lett. **80**, 5180 (1998).